

Light-Induced Valleytronics in Pristine Graphene

Mrudul M. S.,¹ Álvaro Jiménez-Galán,² Misha Ivanov,² and Gopal Dixit^{1,*}

¹*Department of Physics, Indian Institute of
Technology Bombay, Powai, Mumbai 400076, India*

²*Max-Born Institut, Max-Born Straße 2A, 12489 Berlin, Germany*

(Dated: March 16, 2022)

Abstract

It is often assumed that achieving valley selective excitation in pristine graphene with all-optical means is not possible due to the inversion symmetry of the system. Here we demonstrate that both valley-selective excitation and valley-selective high-harmonic generation can be achieved in pristine graphene by using the combination of two counter-rotating circularly polarized fields, the fundamental and its second harmonic. Controlling the relative phase between the two colours allows us to select the valleys where the electron-hole pairs and higher-order harmonics are generated. Present work offers a robust recipe to realise valley-selective electron excitations in materials with zero bandgap and zero Berry curvature.

* gdixit@phy.iitb.ac.in

The realisation of atomically-thin monolayer graphene has led to breakthroughs in fundamental and applied sciences [1, 2]. Charge carriers in graphene are described by the massless Dirac equation and exhibit exceptional transport properties [3], making graphene very attractive for novel electronics applications. One of the most interesting features of graphene and gapped graphene materials is the electron’s extra degree of freedom, the valley pseudospin, associated with populating the local minima \mathbf{K} and \mathbf{K}' in the lowest conduction band of the Brillouin zone. This extra degree of freedom has the potential to encode, process and store quantum information, opening the field of valleytronics [4].

The monolayer graphene, as opposed to gapped graphene materials, presents a fundamental challenge for valleytronics: it has zero bandgap and zero Berry curvature. These aspects are generally considered to be a major impediment for valleytronics. In gapped graphene materials, valley selectivity is achieved by matching the helicity of a circularly polarized pump pulse, resonant to the bandgap, to the sign of the Berry curvature [5–9]. Recently demonstrated [10] sub-cycle manipulation of electron population in \mathbf{K} and \mathbf{K}' valleys of tungsten diselenide, achieved with the combination of a resonant pump pulse locked to the oscillations of the THz control pulse, represents a major milestone. Precise sub-cycle control over the driving light fields opens new opportunities for valleytronics, such as those offered by the new concept of a topological resonance, discovered and analysed in Refs. [11–13]. Single-cycle pulses with the controlled phase of carrier oscillations under the envelope offer a route to valleytronics in gapped graphene-type materials even when such pulses are linearly, not circularly, polarized [14]. It is also possible to avoid the reliance on resonances in gapped graphene-type materials, breaking the symmetry between the \mathbf{K} and \mathbf{K}' valleys via a light-induced topological phase transition, closing the gap in the desired valley [15].

Thus, with its zero bandgap, zero Berry curvature, and identical dispersion near the bottom of the valleys, pristine graphene appears unsuitable for valleytronics – a disappointing conclusion in view of its exceptional transport properties. We show that this generally accepted conclusion is not correct, and that the preferential population of a desired valley can be achieved by tailoring the polarization state of the driving light pulse to the symmetry of the lattice. Our proposal offers an all-optical route to valleytronics in pristine graphene, complementing approaches based on creating a gap by using a heterostructure of graphene with hexagonal boron nitride [16–19], or by adding strain and/or defect engineering [20–23].

We also show valley selectivity of harmonic generation in graphene, and demonstrate

it with the same field as we use for valley-selective electronic excitation. High-harmonic generation (HHG) is a powerful method for probing attosecond electron dynamics in systems as diverse as atoms, molecules [24–29] and solids [30–43]. In solids, high harmonic spectroscopy was used to probe valence electrons [34], atomic arrangement in solids [34–36], defects [44, 45], band dispersion [37–39] and quantum phase transitions [40, 41, 46], and to realise petahertz electronics in solids [34, 42, 43].

The key idea of our approach is illustrated in Fig. 1, which shows graphene in real (a) and reciprocal (b) space, together with the structure of the incident electric field (a) and the corresponding vector potential (b). The field is made by superimposing two counter-rotating circularly polarized colours at the frequencies ω and 2ω . The Lissajous figure for the total electric field is a trefoil, and its orientation is controlled by the relative two-colour phase ϕ , i.e., the two-colour delay. In the absence of the field, the two carbon atoms A and B, in real space, are related by the inversion symmetry. When the field is turned on, this inversion symmetry is broken: the electric field in panel (a) always points from the atom A to the one of the three neighbouring atoms B during the full laser cycle, but not the other way around. If the centre of the Lissajous figure is placed on the atom B, the field points in the middle between its neighbours. One can control this symmetry breaking by rotating the trefoil, interchanging the roles of the atoms A and B. Thus, the bi-circular field offers a simple, all-optical, ultrafast tool to break the inversion symmetry of the graphene lattice in a controlled way. Such controlled symmetry breaking naturally controls the relative excitation probabilities induced by the same laser field in the adjacent \mathbf{K} and \mathbf{K}' valleys of the Brillouin zone.

Panel (b) provides the complementary reciprocal-space perspective. In the laser field, the electron crystal momentum follows $\mathbf{k}(t) = \mathbf{k}_i + \mathbf{A}(t)$, where \mathbf{k}_i is the initial crystal momentum and $\mathbf{A}(t)$ is the laser vector potential, shown in (b) for the electric field shown in (a). The asymmetry between the two valleys with respect to the vector potential is immediately visible.

Panels (c) and (d) provide additional support to this qualitative picture. One can observe that the two field-free valleys, \mathbf{K} and \mathbf{K}' , are only identical near their very bottoms. As soon as one moves away from the bottom, the valleys start to develop the trefoil structure, with \mathbf{K} and \mathbf{K}' being the mirror images of each other. How the symmetry of the vector potential fits into the symmetry of the valley away from their bottoms will control the dynamics and

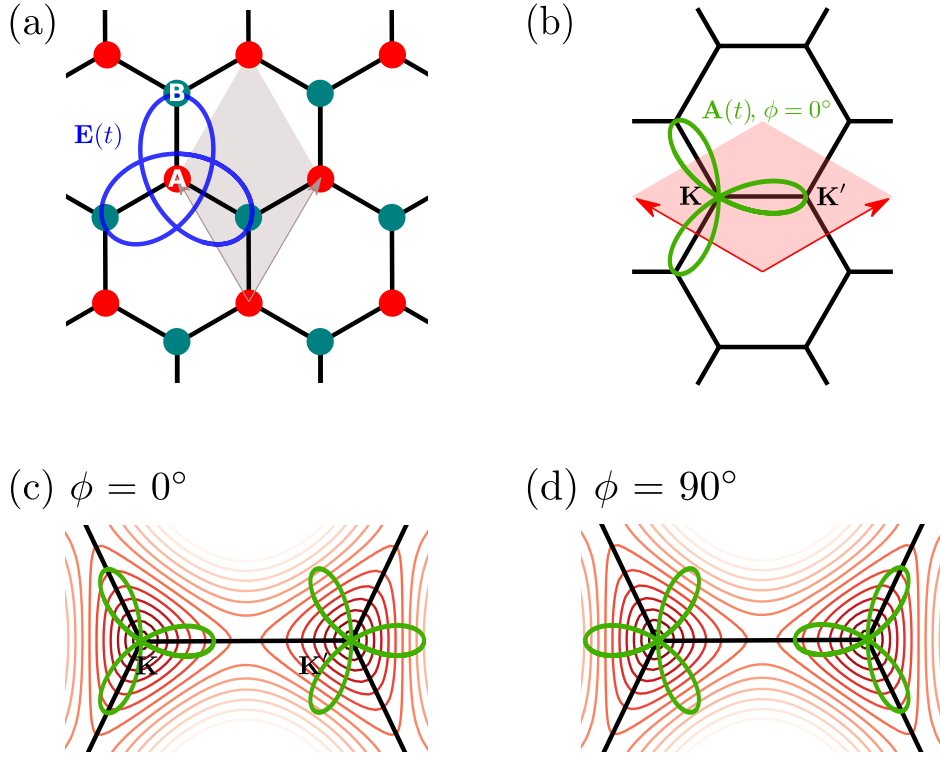


FIG. 1. **Physical mechanism of valley polarization in graphene.** (a) Graphene lattice in the coordinate space, with the Lissajous figure of the bicircular electric field breaking the symmetry between otherwise identical carbon atoms A and B; two-colour phase $\phi = 0$. (b) Optically induced symmetry breaking viewed in the momentum space, the vector potential of the bicircular field is shown for $\phi = 0$. (c, d) Close-up images of the valleys show their asymmetry, leading to different laser-driven dynamics and different excitation rates once the electron leaves the bottom of the valley.

the excitation probability.

In sufficiently strong fields, excitation happens not only at the Dirac point where the gap is equal to zero, but also in its vicinity. For the vector potential in panel (c), the average gap seen by the electron when following the vector potential from the Dirac point in the \mathbf{K} valley, i.e., moving along the trajectory $\mathbf{K} + \mathbf{A}(t)$, is less than in the \mathbf{K}' valley, i.e., when following the trajectory $\mathbf{K}' + \mathbf{A}(t)$. In sufficiently strong and low-frequency fields, such that the bandgap along the trajectories $\mathbf{K} + \mathbf{A}(t)$ and $\mathbf{K}' + \mathbf{A}(t)$ quickly exceeds the photon energy, the excitation probability should therefore be higher in panel (c). For the same

reason, rotating the vector potential as shown in panel (d) should favour population of the \mathbf{K}' valley.

These expectations are confirmed by our numerical simulations. In the simulations, graphene is exposed to the bicircular field with the vector potential

$$\mathcal{A}(t) = \frac{A_0 f(t)}{\sqrt{2}} \left(\left[\cos(\omega t + \phi) + \frac{\mathcal{R}}{2} \cos(2\omega t) \right] \hat{\mathbf{e}}_x + \left[\sin(\omega t + \phi) - \frac{\mathcal{R}}{2} \sin(2\omega t) \right] \hat{\mathbf{e}}_y \right). \quad (1)$$

Here, $A_0 = F_\omega/\omega$ is the amplitude of the vector potential for the fundamental field, F_ω is its strength, $f(t)$ is the temporal envelope of the driving field, ϕ is the sub-cycle phase difference between the two fields, and \mathcal{R} is the ratio of the electric field strengths for the two fields, leading to $\mathcal{R}/2$ ratio for the amplitudes of the vector potentials. The amplitude of the fundamental field was varied up to $F_\omega = 15$ MV/cm, leading to the maximum fundamental intensity 3×10^{11} W/cm², with the fundamental wavelength $\lambda = 6\mu\text{m}$. This laser intensity is lower than the one used in HHG in graphene experimentally [47] and is below the damage threshold. We have also varied \mathcal{R} , using $\mathcal{R} = 1$ and $\mathcal{R} = 2$. A pulse duration of 145 femtosecond with sin-square envelope is employed in this work. Our findings are valid for a broad range of wavelengths and field intensities. To obtain the total population of the different valleys, we have integrated the momentum-resolved population over the sections shown in Fig. 2(a).

To quantify the amount of the valley polarisation, we used the valley asymmetry parameter defined as

$$\eta = \frac{n_c^{\mathbf{K}'} - n_c^{\mathbf{K}}}{(n_c^{\mathbf{K}'} + n_c^{\mathbf{K}})/2}, \quad (2)$$

where $n_c^{\mathbf{K}'}$ and $n_c^{\mathbf{K}}$ are electron populations at the end of the laser pulse in the conduction band around \mathbf{K}' and \mathbf{K} valleys, respectively.

Fig. 2(b) shows the asymmetry in the populations of the \mathbf{K} and \mathbf{K}' valleys as a function of the two-colour phase ϕ , for several values of the fundamental field amplitude and $\mathcal{R} = 2$. Substantial contrast between the two valleys is achieved once the excitations leave the bottom of the Dirac cone, with values as high as $\pm 36\%$ for $\phi = 0^\circ, 90^\circ$, and no asymmetry at $\phi = 45^\circ$. The higher-populated valley is the one where the vector potential “fits” better into the shape of the valley, minimizing the bandgap along the electron trajectory in the momentum space. The same results are obtained when simultaneously changing the helicities of both driving fields, Fig. 2(c, d). The asymmetry in the valley population is negligible up to an intensity of 2×10^{11} W/cm² and gradually increases with intensity [Fig. 2 (b)]. This

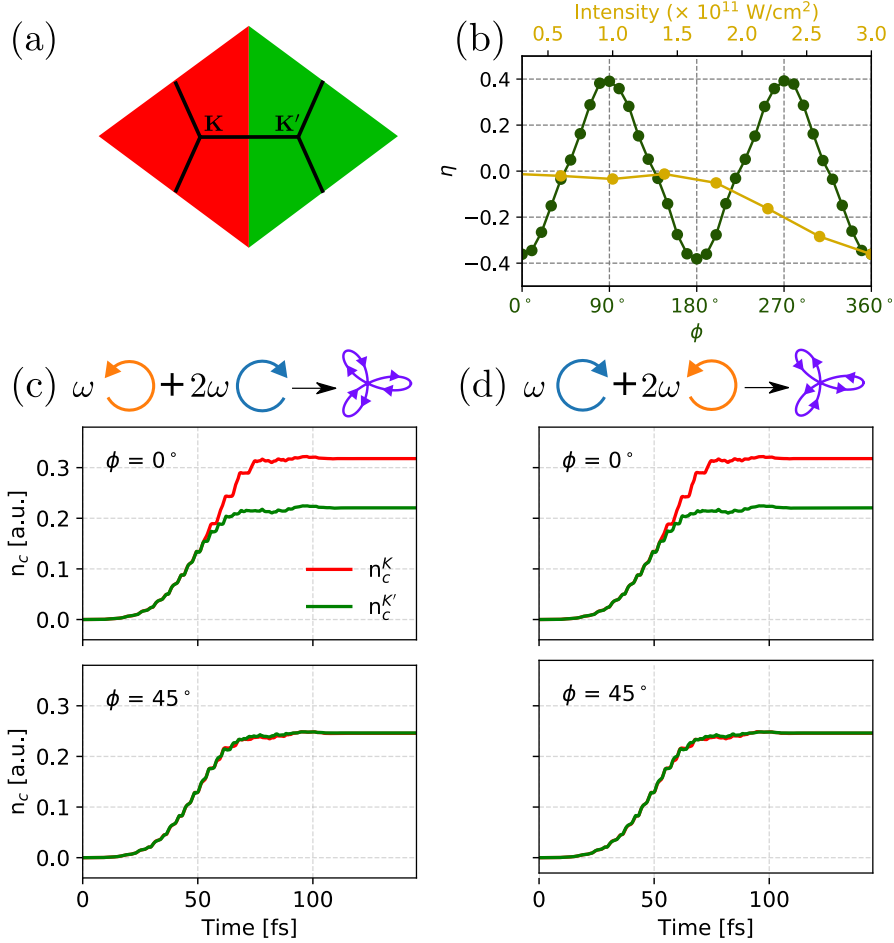


FIG. 2. **Valley asymmetry around two valleys \mathbf{K}' and \mathbf{K} .** (a) Separation of the Brillouin zone into the \mathbf{K}' and \mathbf{K} valleys. (b) Asymmetry in the valley-resolved populations in the conduction band as a function of ϕ (green line with an intensity 3×10^{11} W/cm 2), and laser intensity (yellow line with $\phi = 0^\circ$) for a laser with wavelength of $6 \mu\text{m}$, $\mathcal{R} = 2$, and a dephasing time of 10 fs . (c, d) Excitation dynamics during the laser pulse for $\phi = 0^\circ, 45^\circ$: switching the helicities of both the fields simultaneously does not change the outcome.

shows that the valley asymmetry is observed only when the laser pulse is able to drive the electrons to the anisotropic part of the conduction band.

The current generated by the electron injection into the conduction band valleys is accompanied by harmonic radiation and makes substantial contribution to the lower order harmonics, such as H4 and H5 for our two-colour driver. These harmonics are stronger whenever the dispersion $\epsilon(\mathbf{k})$ is more nonlinear. In this respect, for the electrons following the trajectories $\mathbf{K} + \mathbf{A}(t)$ and $\mathbf{K}' + \mathbf{A}(t)$, the current-driven high harmonic generation from

the \mathbf{K}' valley is preferred for the vector potential in Fig. 1(c). Conversely, for the vector potential in Fig. 1(d) low-order, current-driven harmonic generation should be preferred from the \mathbf{K} valley. Indeed, following the vector potential, the electron is driven against the steeper walls in the \mathbf{K}' valley in panel (c) and against the steeper walls in the \mathbf{K} valley in panel (d).

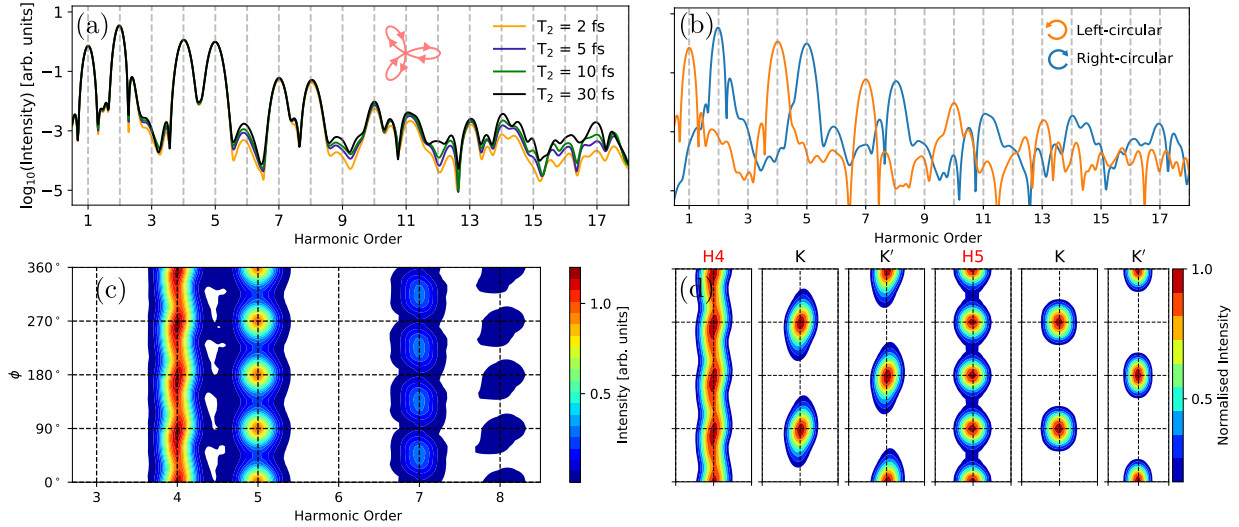


FIG. 3. Valley polarization in high-harmonic emission driven by a bicircular field in graphene. (a) Harmonic spectrum for different dephasing times, for the vector potential shown in the inset ($\phi = 0$); (b) Polarisation-resolved high harmonic emission, for left-handed circularly polarised fundamental (orange) and right-handed circularly polarised second harmonic (blue). Alternating harmonics follow alternating helicities: $3n + 1$ follow the fundamental, $3n + 2$ follow the second harmonic, the $3n$ harmonics missing due to symmetry. (c) Harmonic emission as a function of the two-colour phase ϕ . (d) Valley polarization of H4 and H5 as a function of the two-colour phase. The total field is identical for $\phi = 0^\circ$ and $\phi = 180^\circ$ owing to the threefold symmetry.

These qualitative expectations are also confirmed by our numerical simulations, shown in Fig. 3. The same laser parameters used in Fig. 2 are used in this simulation.

In general, the interband and intraband harmonic emission mechanisms in graphene are coupled [48–50], except at low electric fields [50], leading to a complex interplay between the interband and intraband emission mechanisms. The former should be more sensitive to the dephasing than the latter. To this end, we have calculated the the harmonic spectrum for

different dephasing times T_2 , see Fig. 3(a). We find that the harmonic emission is essentially T_2 -independent, until at least H13, suggesting that the intraband emission mechanism is generally dominant.

Fig. 3(b) shows polarisation-resolved high-harmonic spectrum. The $(3n + 1)$ harmonics follow the polarisation of the ω pulse (left-handed circular polarisation), whereas $(3n + 2)$ harmonics follow the polarisation of the 2ω pulse (right-handed circular polarisation), while $3n$ harmonics are missing, just like in atomic media [51]. In this context, we note that while harmonic generation with single-colour circularly polarized drivers is forbidden in atoms, such selection rules do not generally arise in solids [31]. However, the ellipticity-dependence studies on graphene show very weak harmonic yield for drivers with higher ellipticity [47–49], as we have also observed. As in atoms, application of bicircular fields allows for efficient generation of circularly polarized harmonics in graphene.

Fig. 3(c) shows the dependence of harmonic generation on the orientation of the vector potential relative to the structure of the Brillouin zone. As expected, the total harmonic yield is modulated as the trefoil is rotated, with the lower-order current-driven harmonics H4 and H5 following the expected pattern, maximizing when the electrons are driven into the steeper walls in either the \mathbf{K}' or \mathbf{K} valley.

The contribution of different valleys to H4 and H5 as a function of the field orientation is presented in Figs. 3(d). Consistent with the qualitative analysis above, maximum harmonic contribution of the \mathbf{K}' valley corresponds to the vector potential orientations such as shown in Fig. 1(c), while the maximum contribution of the \mathbf{K} valley corresponds to the vector potential orientations such as shown in Fig. 1(d). Therefore, we are able to control the valley-polarisation of the harmonics by controlling the two-colour phase ϕ . We have also checked that these results do not depend on the specific directions of rotation of the two driving fields. That is, we find the same results when simultaneously changing the helicities of both driving fields.

Thus, valley polarisation in both electronic excitation and harmonic generation can be achieved in pristine graphene by tailoring the Lissajous figure of the driving pulse to the symmetry of the graphene lattice. This allows one to both break the inversion symmetry between the adjacent carbon atoms and also exploit the anisotropic regions in the valleys, taking advantage of the fact that the energy landscape of the valleys are mirror images of each other. Present work opens an avenue for a new regime of valleytronics in pristine

graphene and similar materials with zero bandgap and zero Berry curvature.

METHODS

In the simulations, we used the nearest-neighbour tight-binding approximation to obtain the ground state of graphene with a hopping-energy of 2.7 eV [52]. The lattice parameter of graphene is chosen to be 2.46 Å. The resultant band-structure has zero band-gap with linear dispersion near the two points in the Brillouin zone known as \mathbf{K} and \mathbf{K}' points.

The density matrix approach was used to follow the electron dynamics in graphene. Time-evolution of density matrix element, $\rho_{mn}^{\mathbf{k}}$, was performed using semiconductor Bloch equations within the Houston basis $|n, \mathbf{k} + \mathcal{A}(t)\rangle$ as [53, 54]

$$\partial_t \rho_{mn}^{\mathbf{k}} = -i\epsilon_{mn}^{\mathbf{k}+\mathcal{A}(t)} \rho_{mn}^{\mathbf{k}} - (1 - \delta_{mn}) \frac{\rho_{mn}^{\mathbf{k}}}{T_2} + i\mathcal{F}(t) \cdot \left[\sum_l \left(\mathbf{d}_{ml}^{\mathbf{k}+\mathcal{A}(t)} \rho_{ln}^{\mathbf{k}} - \mathbf{d}_{ln}^{\mathbf{k}+\mathcal{A}(t)} \rho_{ml}^{\mathbf{k}} \right) \right]. \quad (3)$$

Here, $\epsilon_{mn}^{\mathbf{k}}$ and $\mathbf{d}_{mn}^{\mathbf{k}}$ are, respectively, the band-gap energy and the dipole-matrix elements between m and n energy-bands at \mathbf{k} . Dipole matrix elements were calculated as $\mathbf{d}_{mn}^{\mathbf{k}} = -i\langle u_m^{\mathbf{k}} | \nabla_{\mathbf{k}} | u_n^{\mathbf{k}} \rangle$, where $u_n^{\mathbf{k}}$ is the Bloch function corresponding to the total wavefunction. $\mathcal{F}(t)$ and $\mathcal{A}(t)$ are, respectively, the electric field and vector potential of the laser field and are related as $\mathcal{F}(t) = -\partial\mathcal{A}(t)/\partial t$. A phenomenological term accounting for the decoherence is added with a constant dephasing time T_2 . Conduction band population relaxation was neglected [55].

The total current was calculated as

$$\mathbf{J}(\mathbf{k}, t) = \sum_{m,n} \rho_{mn}^{\mathbf{k}}(t) \mathbf{p}_{nm}^{\mathbf{k}+\mathcal{A}(t)}. \quad (4)$$

Here, $\mathbf{p}_{nm}^{\mathbf{k}}$ are the momentum matrix elements, obtained as $\mathbf{p}_{nm}^{\mathbf{k}} = \langle n, \mathbf{k} | \nabla_{\mathbf{k}} \hat{H}_{\mathbf{k}} | m, \mathbf{k} \rangle$. The off-diagonal elements of momentum and dipole-matrix elements are related as $\mathbf{d}_{mn}^{\mathbf{k}} = i\mathbf{p}_{mn}^{\mathbf{k}}/\epsilon_{mn}^{\mathbf{k}}$.

Finally, the harmonic spectrum was determined from the Fourier-transform of the time-derivative of the total current as

$$\mathcal{I}(\omega) = \left| \mathcal{FT} \left(\frac{d}{dt} \left[\int_{BZ} \mathbf{J}(\mathbf{k}, t) d\mathbf{k} \right] \right) \right|^2. \quad (5)$$

Here, integration is performed over the entire Brillouin zone.

DATA AVAILABILITY

The datasets that support the findings of this study are available from the corresponding authors on reasonable request.

COMPETING FINANCIAL INTERESTS

The authors declare no competing financial interests.

ACKNOWLEDGMENTS

M.I. acknowledges support from the Deutsche Forschungsgemeinschaft (DFG) Quantum Dynamics in Tailored Intense Fields (QUTIF) grant. M.I. and A. J-G acknowledge support of the FET-Open Optologic grant. G. D. acknowledges support from Science and Engineering Research Board (SERB) India (Project No. ECR/2017/001460).

-
- [1] Novoselov, K. S. *et al.* Electric field effect in atomically thin carbon films. *Science* **306**, 666–669 (2004).
- [2] Geim, A. K. Graphene: status and prospects. *Science* **324**, 1530–1534 (2009).
- [3] Neto, A. H. C., Guinea, F., Peres, N. M. R., Novoselov, K. S. & Geim, A. K. The electronic properties of graphene. *Reviews of Modern Physics* **81**, 109 (2009).
- [4] Vitale, S. A. *et al.* Valleytronics: opportunities, challenges, and paths forward. *Small* **14**, 1801483 (2018).
- [5] Schaibley, J. R. *et al.* Valleytronics in 2d materials. *Nature Reviews Materials* **1**, 16055 (2016).
- [6] Mak, K. F., He, K., Shan, J. & Heinz, T. F. Control of valley polarization in monolayer mos2 by optical helicity. *Nature Nanotechnology* **7**, 494–498 (2012).
- [7] Jones, A. M. *et al.* Optical generation of excitonic valley coherence in monolayer wse2. *Nature Nanotechnology* **8**, 634–638 (2013).
- [8] Gunlycke, D. & White, C. T. Graphene valley filter using a line defect. *Physical Review Letters* **106**, 136806 (2011).
- [9] Xiao, D., Liu, G. B., Feng, W., Xu, X. & Yao, W. Coupled spin and valley physics in monolayers of mos 2 and other group-vi dichalcogenides. *Physical Review Letters* **108**, 196802 (2012).
- [10] Langer, F. *et al.* Lightwave valleytronics in a monolayer of tungsten diselenide. *Nature* **557**, 76 (2018).
- [11] Motlagh, S. A. O., Nematollahi, F., Apalkov, V. & Stockman, M. I. Topological resonance and single-optical-cycle valley polarization in gapped graphene. *Physical Review B* **100**, 115431 (2019).
- [12] Motlagh, S. A. O., Wu, J. S., Apalkov, V. & Stockman, M. I. Femtosecond valley polarization and topological resonances in transition metal dichalcogenides. *Physical Review B* **98**, 081406 (2018).
- [13] Keldarsh, H. K., Apalkov, V. & Stockman, M. I. Attosecond strong-field interferometry in graphene: Chirality, singularity, and berry phase. *Physical Review B* **93**, 155434 (2016).
- [14] Jiménez-Galán, Á., Silva, R., Smirnova, O. & Ivanov, M. Sub-cycle valleytronics: control of valley polarization using few-cycle linearly polarized pulses. *arXiv preprint arXiv:2005.10196*

- (2020).
- [15] Jiménez-Galán, Á., Silva, R. E. F., Smirnova, O. & Ivanov, M. Lightwave topology for strong-field valleytronics. arXiv arXiv-1910 (2019).
 - [16] Gorbachev, R. V. et al. Detecting topological currents in graphene superlattices. Science **346**, 448–451 (2014).
 - [17] Yankowitz, M. et al. Emergence of superlattice dirac points in graphene on hexagonal boron nitride. Nature Physics **8**, 382–386 (2012).
 - [18] Hunt, B. et al. Massive dirac fermions and hofstadter butterfly in a van der waals heterostructure. Science **340**, 1427–1430 (2013).
 - [19] Rycerz, A., Tworzydło, J. & Beenakker, C. W. J. Valley filter and valley valve in graphene. Nature Physics **3**, 172–175 (2007).
 - [20] Grujić, M. M., Tadić, M. Ž. & Peeters, F. M. Spin-valley filtering in strained graphene structures with artificially induced carrier mass and spin-orbit coupling. Physical Review Letters **113**, 046601 (2014).
 - [21] Settnes, M., Power, S. R., Brandbyge, M. & Jauho, A. P. Graphene nanobubbles as valley filters and beam splitters. Physical Review Letters **117**, 276801 (2016).
 - [22] Faria, D., León, C., Lima, L. R. F., Latgé, A. & Sandler, N. Valley polarization braiding in strained graphene. Physical Review B **101**, 081410 (2020).
 - [23] Xiao, D., Yao, W. & Niu, Q. Valley-contrasting physics in graphene: magnetic moment and topological transport. Physical Review Letters **99**, 236809 (2007).
 - [24] Lein, M. Molecular imaging using recolliding electrons. Journal of Physics B: Atomic, Molecular and Optical Physics **40**, R135 (2007).
 - [25] Baker, S. et al. Probing proton dynamics in molecules on an attosecond time scale. Science **312**, 424–427 (2006).
 - [26] Smirnova, O. et al. High harmonic interferometry of multi-electron dynamics in molecules. Nature **460**, 972–977 (2009).
 - [27] Shafir, D. et al. Resolving the time when an electron exits a tunnelling barrier. Nature **485**, 343–346 (2012).
 - [28] Bruner, B. D. et al. Multidimensional high harmonic spectroscopy of polyatomic molecules: detecting sub-cycle laser-driven hole dynamics upon ionization in strong mid-ir laser fields. Faraday discussions **194**, 369–405 (2016).

- [29] Wörner, H. J., Bertrand, J. B., Kartashov, D. V., Corkum, P. B. & Villeneuve, D. M. Following a chemical reaction using high-harmonic interferometry. Nature **466**, 604–607 (2010).
- [30] Kruchinin, S. Y., Krausz, F. & Yakovlev, V. S. Colloquium: Strong-field phenomena in periodic systems. Reviews of Modern Physics **90**, 021002 (2018).
- [31] Ghimire, S. et al. Observation of high-order harmonic generation in a bulk crystal. Nature Physics **7**, 138–141 (2011).
- [32] Schubert, O. et al. Sub-cycle control of terahertz high-harmonic generation by dynamical bloch oscillations. Nature Photonics **8**, 119 (2014).
- [33] Langer, F. et al. Lightwave-driven quasiparticle collisions on a subcycle timescale. Nature **533**, 225 (2016).
- [34] Lakhotia, H. et al. Laser picoscopy of valence electrons in solids. Nature **583**, 55–59 (2020).
- [35] You, Y. S., Reis, D. A. & Ghimire, S. Anisotropic high-harmonic generation in bulk crystals. Nature Physics **13**, 345–349 (2017).
- [36] Mrudul, M. S., Pattanayak, A., Ivanov, M. & Dixit, G. Direct numerical observation of real-space recollision in high-order harmonic generation from solids. Physical Review A **100**, 043420 (2019).
- [37] Luu, T. T. et al. Extreme ultraviolet high-harmonic spectroscopy of solids. Nature **521**, 498 (2015).
- [38] Lanin, A. A., Stepanov, E. A., Fedotov, A. B. & Zheltikov, A. M. Mapping the electron band structure by intraband high-harmonic generation in solids. Optica **4**, 516–519 (2017).
- [39] Vampa, G. et al. All-optical reconstruction of crystal band structure. Physical Review Letters **115**, 193603 (2015).
- [40] Silva, R. E. F., Blinov, I. V., Rubtsov, A. N., Smirnova, O. & Ivanov, M. High-harmonic spectroscopy of ultrafast many-body dynamics in strongly correlated systems. Nature Photonics **12**, 266 (2018).
- [41] Bauer, D. & Hansen, K. K. High-harmonic generation in solids with and without topological edge states. Physical Review Letters **120**, 177401 (2018).
- [42] Reimann, J. et al. Subcycle observation of lightwave-driven dirac currents in a topological surface band. Nature **562**, 396–400 (2018).
- [43] Garg, M. et al. Multi-petahertz electronic metrology. Nature **538**, 359 (2016).

- [44] Siviş, M. *et al.* Tailored semiconductors for high-harmonic optoelectronics. Science **357**, 303–306 (2017).
- [45] Mrudul, M. S., Tancogne-Dejean, N., Rubio, A. & Dixit, G. High-harmonic generation from spin-polarised defects in solids. npj Computational Materials **6**, 1–9 (2020).
- [46] Silva, R. E. F., Jiménez-Galán, Á., Amorim, B., Smirnova, O. & Ivanov, M. Topological strong-field physics on sub-laser-cycle timescale. Nature Photonics **13**, 849–854 (2019).
- [47] Yoshikawa, N., Tamaya, T. & Tanaka, K. High-harmonic generation in graphene enhanced by elliptically polarized light excitation. Science **356**, 736–738 (2017).
- [48] Taucer, M. *et al.* Nonperturbative harmonic generation in graphene from intense midinfrared pulsed light. Physical Review B **96**, 195420 (2017).
- [49] Liu, C., Zheng, Y., Zeng, Z. & Li, R. Driving-laser ellipticity dependence of high-order harmonic generation in graphene. Physical Review A **97**, 063412 (2018).
- [50] Al-Naib, I., Sipe, J. E. & Dignam, M. M. High harmonic generation in undoped graphene: Interplay of inter-and intraband dynamics. Physical Review B **90**, 245423 (2014).
- [51] Fleischer, A., Kfir, O., Diskin, T., Sidorenko, P. & Cohen, O. Spin angular momentum and tunable polarization in high-harmonic generation. Nature Photonics **8**, 543–549 (2014).
- [52] Reich, S., Maultzsch, J., Thomsen, C. & Ordejón, P. Tight-binding description of graphene. Physical Review B **66**, 035412 (2002).
- [53] Golde, D., Meier, T. & Koch, S. W. High harmonics generated in semiconductor nanostructures by the coupled dynamics of optical inter-and intraband excitations. Physical Review B **77**, 075330 (2008).
- [54] Floss, I. *et al.* Ab initio multiscale simulation of high-order harmonic generation in solids. Physical Review A **97**, 011401 (2018).
- [55] Hwang, E. H. & Sarma, S. D. Single-particle relaxation time versus transport scattering time in a two-dimensional graphene layer. Physical Review B **77**, 195412 (2008).